Electronic Supplementary Material (ESI) for Journal of Materials Chemistry A.

Supporting Information

Enhanced Li-ion intercalation kinetics and lattice oxygen stability in single-crystalline Ni-rich Co-poor layered cathodes

Hujun Zhang[a], Li Qin[a], Michal Sedlacik[c], Petr Saha[c], Qilin Cheng[a*], Haifeng Yu[a,b*], Hao Jiang[a,b]

a Shanghai Engineering Research Center of Hierarchical Nanomaterials, School of Materials Science and Engineering, East China University of Science and Technology, Shanghai 200237, China

b Key Laboratory for Ultrafine Materials of Ministry of Education, School of Chemical Engineering, East China University of Science and Technology, Shanghai 200237, China

c Centre of Polymer Systems, University Institute, Tomas Bata University in Zlín, Trida T. Bati 5678, 760 01, Zlín, Czech Republic

*Corresponding author, Tel.: +86-21-64250949, Fax: +86-21-64250624

E-mail: chengql@ecust.edu.cn (Prof. Q. Cheng), hfyu@ecust.edu.cn (Dr. H. Yu)

Part I: Supporting Experimental Section

1. Material characterization

The morphology and microstructure of the samples were characterized using scanning electron microscopy (SEM, Hitachi S-4800) and field emission transmission electron microscopy (TEM, Talos F200X). The atomic percentages of all samples were tested by energy dispersive spectrometry spectra (EDS, Helios G4 UC). The crystalline phases of the single-crystalline Ni-rich cathodes were investigated using an X-ray diffractometer (XRD, Ultima IV) and crystallography data analysis software (GSAS) refinement. The chemical composition of the samples was analyzed using high-performance inductively coupled plasma-mass spectrometry (ICP-MS, NexION 2000-(A-10)). The surface chemistry before and after cathodic cycling was investigated using an X-ray photoelectron spectrometer (XPS, ESCALAB 250Xi), and the resulting data were calibrated using the C1s peak (284.8 eV). Oxygen vacancy defects in the cathode material were tested using electron paramagnetic resonance spectroscopy (EPR, EMX-8/2.7). An *in situ* differential electrochemical mass spectrometer (DEMS, QAS 100) was used to determine trace gases generated during the electrochemical charging and discharging of half-cells in real-time. The carrier gas species was Ar, and the flow rate of Ar was 0.9 mL/min.

2. Electrochemical measurements

All cathodes underwent testing for Coulombic efficiency, rate performance, and cycling performance in a CR2016 coin cell using a LAND battery tester (CT2001A, 1 C = 180 mA g^{-1}). Cyclic voltammetry (CV) curves and electrochemical impedance spectroscopy (EIS) tests were conducted using a Metrohm electrochemical workstation (Autolab PGSTAT302N) at an experimental frequency of 100 kHz-0.01 Hz. The galvanostatic intermittent titration technique (GITT) test involved charging/discharging the battery at 0.1 C for 20 min, followed by a 1 h rest at open circuit. To assemble the button cell, the positive active material (80 wt%) was mixed with the conductive agent (Super-P, 10 wt%) and the binder polyvinylidene fluoride (PVDF, 10 wt%) through stirring, and then uniformly coated onto an aluminum foil using N-methyl-2-pyrrolidone (NMP) as a solvent. The positive electrode sheets were loaded with a mass of 1.7-2.5 mg cm^{-2}. The electrolyte used was 1.2 M $LiPF_6$ in ethylene carbonate (EC)/ethyl methyl carbonate (EMC) (V_{EC}: V_{EMC} = 3:7) with 2 wt% vinylene carbonate (VC), and the cell separator was a polypropylene membrane (Celgard 2400). The assembly process was carried out in an argon glove box with H_2O and O_2 levels below 0.01 ppm. The rate performance and cycle performance tests of pouch full-cell were conducted using the NEWARE battery tester (BTS4000). For the assembly of the pouch full-cell, the cathode electrode consisted of active material (BA-NCM85/B-NCM85/NCM85/A-NCM85), polyvinylidene fluoride (PVDF), conductive agent carbon black (Super-P), and carbon nanotubes (CNT) in a weight ratio of 94:3:1.5:1.5. The mass loading of the negative (artificial graphite) and positive electrodes was 7.5 mg cm^{-2} and 12.0 mg cm^{-2}, respectively, with an N/P ratio of 1.1:1. Then the cut cathode (4.1×6.3 cm^2), anode (4.3×6.5 cm^2) and diaphragm (Celgard 2400) are stacked and wound into a square cell of Li-ion battery in sequence and welded with battery tab. Afterwards, the aluminum-plastic film was thermally encapsulated into a square cell of Li-ion battery, and the electrolyte (1.2 M $LiPF_6$ in EC/EMC (V_{EC} : V_{EMC}=3 : 7)/2 wt% VC) was filled into an argon-filled glove box. After vacuum sealing, formation, vacuum second sealing, and grading, a pouch-type full-cell with a capacity of about 50 mAh can be obtained.

3 The testing process and calculation equation of GITT measurement

For the GITT measurement, the assembled coin-type half-cells were firstly galvanostatic charge/discharged at a constant current of 0.1 C for 2 cycles. Subsequently, the charging/discharging interval was set as 20 minutes, and the open circuit lasted 1 h to allow the cell voltage to relax to its quasi-equilibrium state. The change in the steady-state voltage ΔE_s is obtained by subtracting the original voltage (E_0) from the steady-state voltage (E_s). The cell voltage increases during the current flux and the total change of cell voltage ΔE_τ can be obtained by calculating the voltage drop. Meanwhile, the process of the chemical diffusion is assumed to obey Fick's second law of diffusion. With a series of simplifications, for sufficient time interval ($\tau \ll L^2/D_{Li^+}$), the equation of D_{Li^+} can be written as (Equation 1):

$$D_{Li^+} = \frac{4}{\pi}\left(\frac{m_B V_m}{M_B A}\right)^2 \left(\frac{\Delta E_s}{\tau\left(\frac{dE_\tau}{\sqrt{\tau}}\right)}\right)^2 \left(\tau \ll \frac{L^2}{D_{Li^+}}\right) \qquad (1)$$

where V_m is the molar volume of active materials, M_B and m_B are the molecular weight and mass of the host oxide, respectively, and A is the total contact area between the electrolyte and the electrode, L is the thickness of the electrode. If sufficiently small currents and short time intervals are employed, the cell voltage is a linear function of the square root of τ, Equation 1 can be further simplified as (Equation 2):

$$D_{Li^+} = \frac{4L^2}{\pi\tau}\left(\frac{\Delta E_s}{\Delta E_\tau}\right)^2 \left(\tau \ll \frac{L^2}{D_{Li^+}}\right) \qquad (2)$$

where ΔE_s is the value of subtracting the original voltage (E_0) from the steady-state voltage (E_s). ΔE_τ is the change in the total temporary potential during the application of current in τ, L is the thickness of the electrode. [1,2]

Part II: Supporting Figures

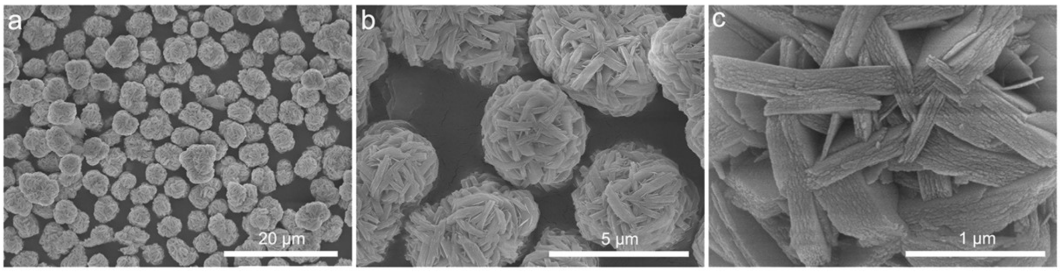

Fig. S1. (a-b) SEM images of $Ni_{0.85}Co_{0.05}Mn_{0.10}(OH)_2$.

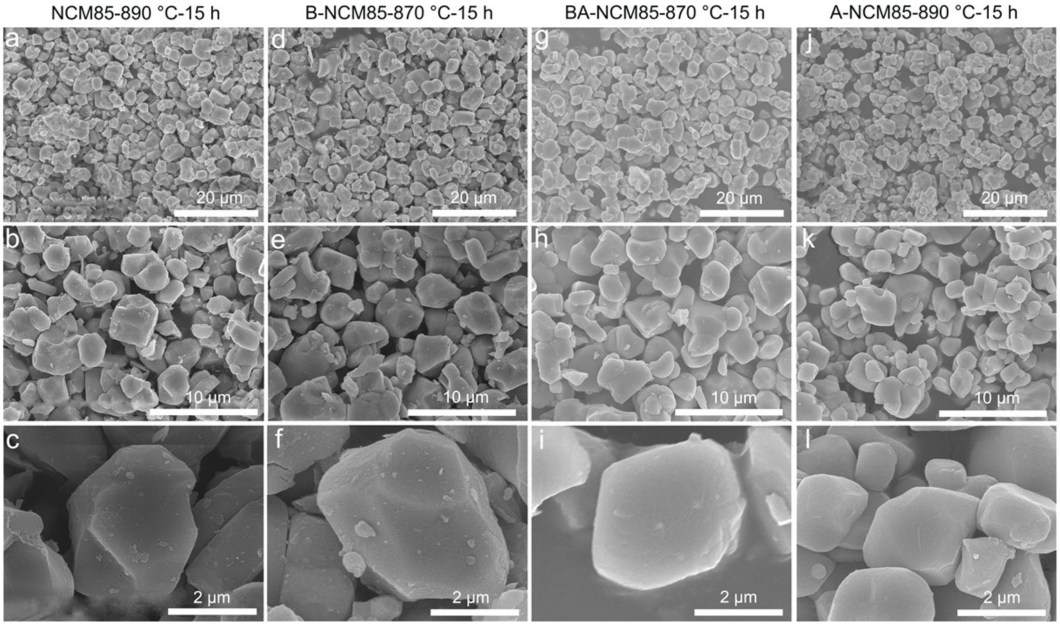

Fig. S2. SEM images of (a-c) NCM85, (d-f) B-NCM85, (g-i) BA-NCM85, and (j-l) A-NCM85.

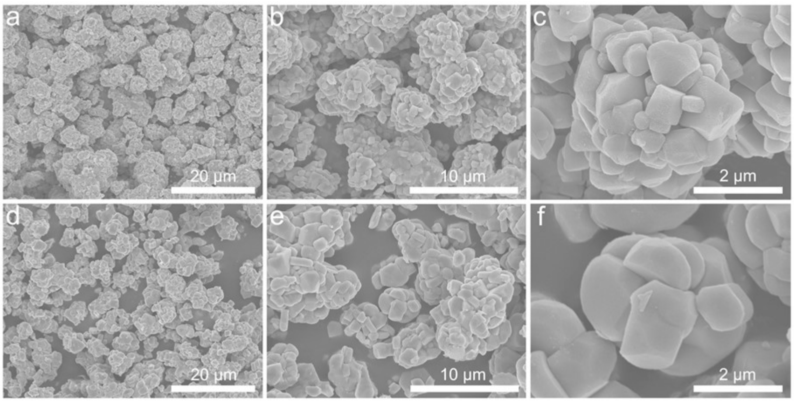

Fig. S3. SEM images of (a-c) NCM85 (870℃-15h) and (d-f) NCM85 (880℃-15h).

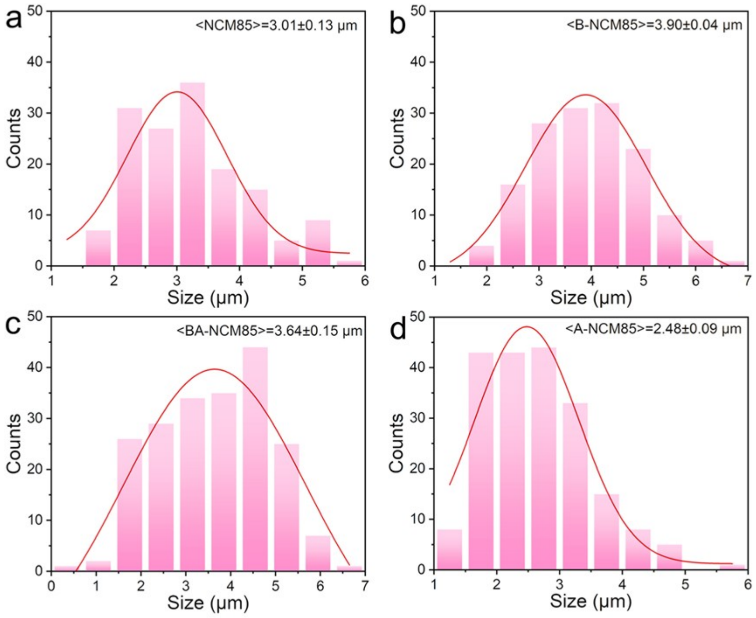

Fig. S4. Statistical analysis of single-crystalline size distribution of (a) NCM85, (b) B-NCM85, (c) BA-NCM85, and (d) A-NCM85.

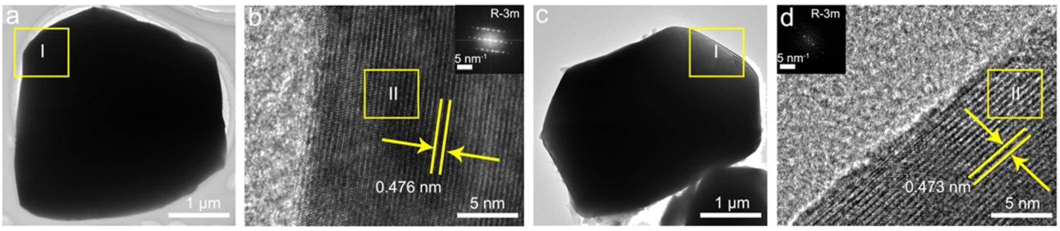

Fig. S5. TEM images of (a) BA-NCM85 and (c) NCM85. HRTEM images of (b) BA-NCM85 and (d) NCM85. FFT images of (b, inset) BA-NCM85 and (d, inset) NCM85.

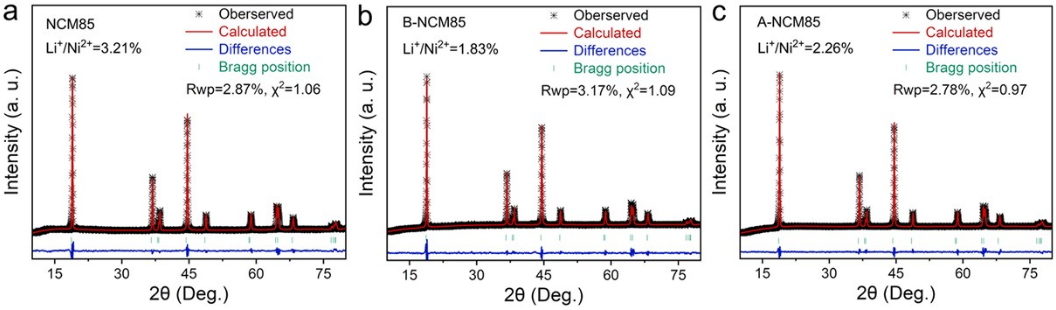

Fig. S6. XRD Rietveld refinement of (a) NCM85, (b) B-NCM85 and (c) A-NCM85.

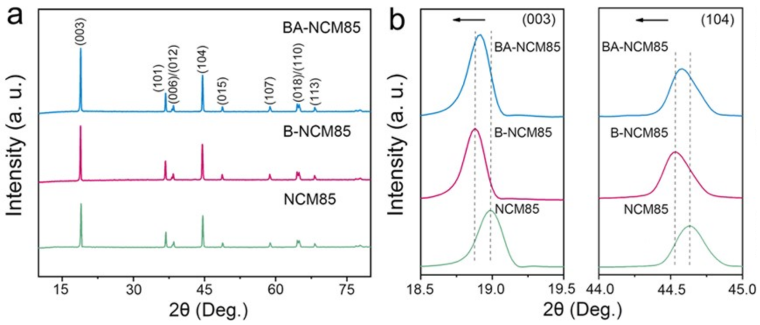

Fig. S7. (a) XRD patterns of pristine NCM85, B-NCM85 and BA-NCM85, (b) with the magnification region of (003) and (104) peak.

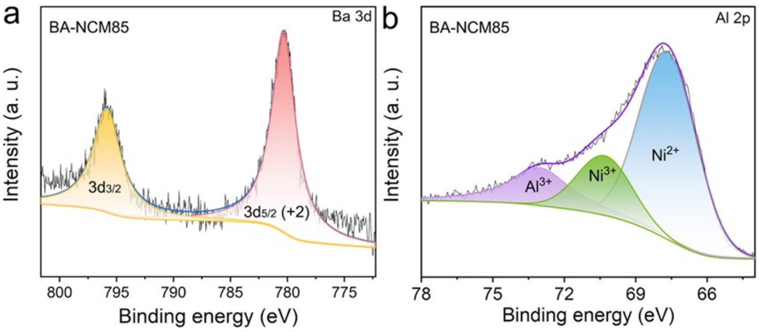

Fig. S8. XPS spectra of (a) Ba 3d and (b) Al 2p for BA-NCM85.

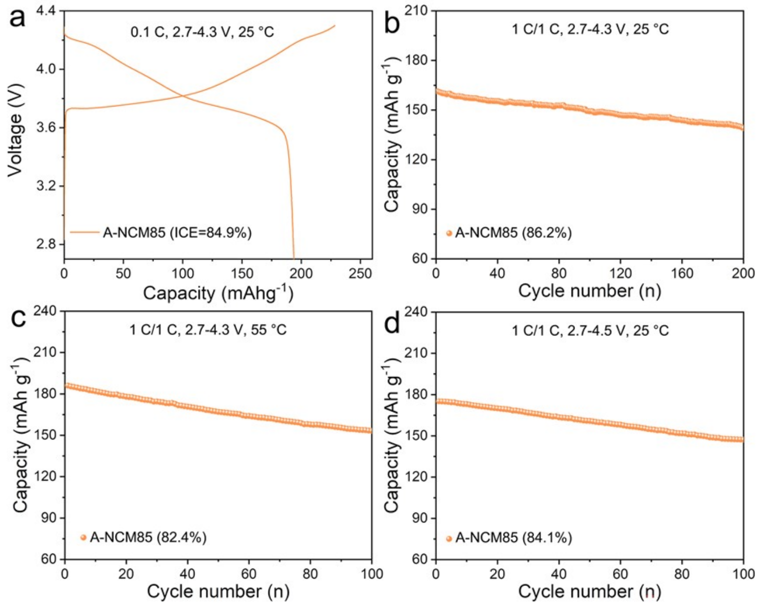

Fig. S9. (a) Initial charge-discharge curves. (b-d) Cycling stability under different conditions of A-NCM85.

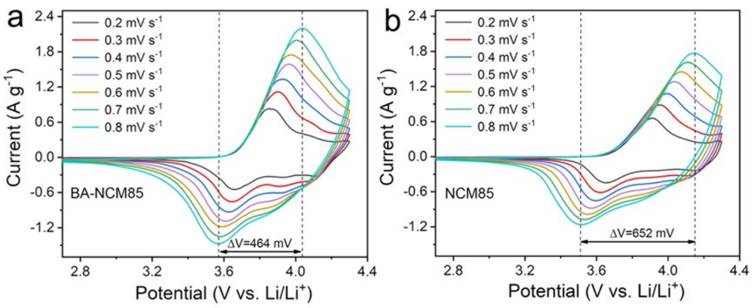

Fig. S10. (a) CV curves at scan rate from 0.2 to 0.8 mV s^{-1} for (a) BA-NCM85 and (b) NCM85.

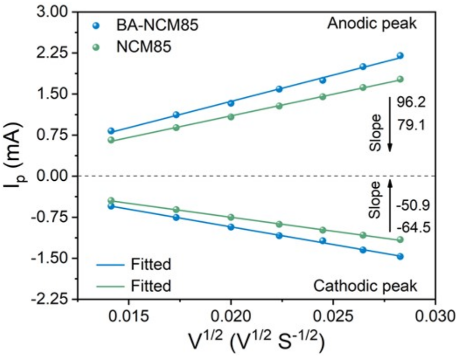

Fig. S11. Linear relationship between the anodic/cathodic peak current (i_p) and the square root of the scan rate ($v^{1/2}$) for BA-NCM85 and NCM85.

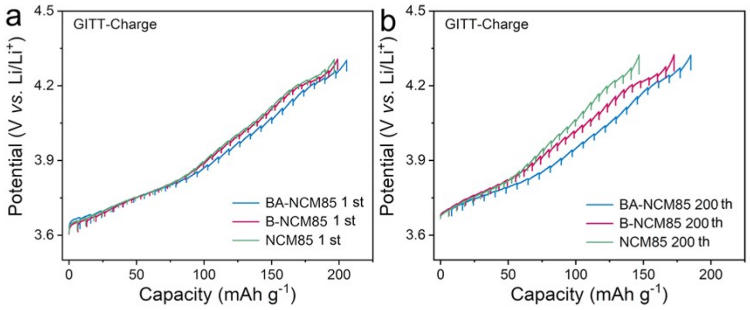

Fig. S12. Charging curves of GITT test at (a) 1 st and (b) 200 th.

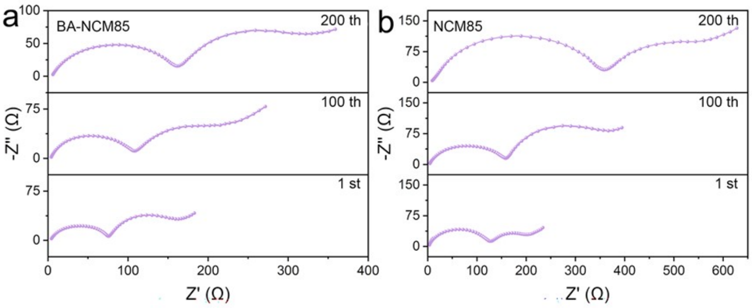

Fig. S13. Nyquist plots of electrochemical impedances at the fully charged state (4.3 V) after different cycle numbers for the (a) BA-NCM85 and (b) NCM85.

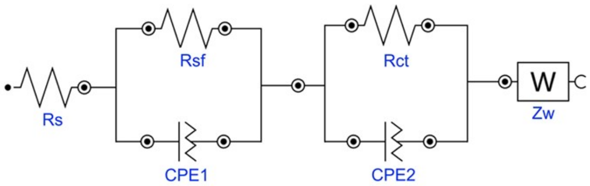

Fig. S14. The equivalent fitting circuit diagram for EIS testing.

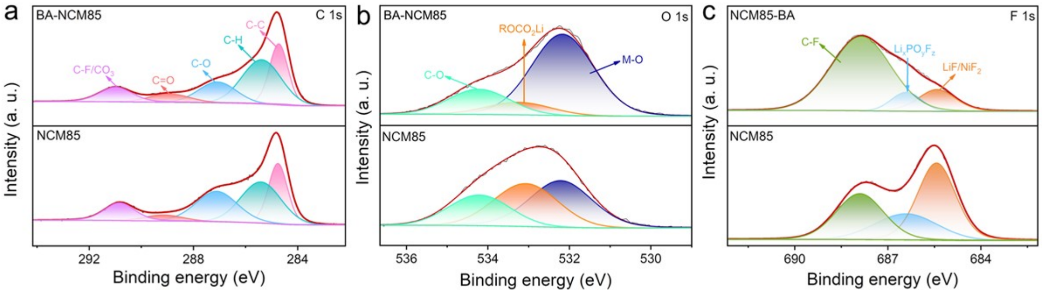

Fig. S15. C 1s, O 1s and F 1s XPS spectra of BA-NCM85 and NCM85 after 200 cycles at 1 C.

Part III: Supporting Tables

Table S1. Rietveld refinement results of XRD data for NCM85, B-NCM85, BA-NCM85 and A-NCM85.

Samples	Lattice parameters				Li^+/Ni^{2+}	wR_p	χ^2
	a(Å)	c(Å)	c/a	V($Å^3$)			
NCM85	2.8776	14.2182	4.9410	101.963	3.21%	2.87%	1.062
B-NCM85	2.8819	14.2360	4.9398	102.394	1.83%	3.17%	1.092
BA-NCM85	2.8826	14.2384	4.9394	102.462	1.55%	3.14%	1.081
A-NCM85	2.8788	14.2197	4.9395	102.042	2.26%	2.78%	0.974

Table S2. ICP-MS results for NCM85, B-NCM85, BA-NCM85 and A-NCM85.

Samples	Mole ratio					
	Li	Ni	Co	Mn	Ba	Al
NCM85	0.991	0.851	0.052	0.097	/	/
B-NCM85	1.005	0.843	0.046	0.102	0.009	/
BA-NCM85	1.003	0.848	0.043	0.101	0.004	0.004
A-NCM85	0.996	0.844	0.045	0.104	/	0.007

Table S3. The R_{sf} and R_{ct} data obtained from the Nyquist plots of different cycle numbers for the BA-NCM85 and NCM85.

Samples	BA-NCM85		NCM85	
cycle number	R_{sf} (Ω)	R_{ct}(Ω)	R_{sf}(Ω)	R_{ct}(Ω)
1 st	76.57	112.76	116.43	131.83
100 th	109.84	196.84	167.22	286.46
200 th	163.86	235.48	365.36	378.98

References

1. H. Yu, H. Zhu, H. Jiang, X. Su, Y. Hu, H. Jiang and C. Li, *Nati. Sci. Rev.*, 2023, **10**, nwac166.

2. H. Yu, Y. Cao, L. Chen, Y. Hu, X. Duan, S. Dai, C. Li and H. Jiang, *Nat. Commun.*, 2021, **12**, 4564.